Broadside Radiating, Low-Profile, Electrically Small, Huygens Dipole Filtenna

Zhentian Wu, *Student Member, IEEE*, Ming-Chun Tang, *Senior Member, IEEE*, and Richard W. Ziolkowski, *Life Fellow, IEEE*

***Abstract*— An electrically small, low-profile, Huygens dipole filtenna is presented that operates near 1.28 GHz. The design incorporates a pair of magnetic and electric near-field resonant parasitic (NFRP) elements and a driven element. Two pairs of interdigitated capacitor structures are integrated into the magnetic NFRP element to produce two deep radiation nulls at both the lower and upper frequency edges of the passband, respectively. The two nulls can be independently controlled to achieve good out-of-band suppression levels. A prototype was fabricated and tested. The measured results, in good agreement with their simulated values, demonstrate that the Huygens dipole filtenna is electrically small (ka = 0.943) and low-profile (0.0385 λ_0), together with enhanced out-of-band rejection performance characteristics. Its fractional bandwidth, broadside realized gain, front-to-back ratio, and overall efficiency values are, respectively, 1.16%, 2.33 dBi, 8.45 dB and 63.1%.**

***Index Terms*—Electrically small antennas, filtennas, Huygens dipole antennas, near-field resonant parasitic elements.**

I. INTRODUCTION

Electrically small, low-profile, Huygens dipole antennas (HDAs) have received increased attention in recent years due to their advantageous radiation performance characteristics. For example, they can exhibit large front-to-back ratios (FTBR) and wide beamwidths without the requirement of additional constructs such as slot structures [1] or reflector elements [2]. A variety of HDAs have been reported to date with different features, i.e., linearly polarized (LP) [3]-[4] and circularly polarized (CP) [5-6] designs, reconfigurable designs [7-8], and non-Foster designs [9]. Benefiting from their remarkable radiation performance, they have been widely applied to a variety of space-limited wireless platforms, e.g., mobile communications [10], and far-field wireless power transfer (WPT) systems [11]. On the other hand, filtennas have the characteristics to suppress the mutual coupling between elements operating at different bands [12-21]. They have been developed for use in a variety of fifth generation (5G) applications [20], including multiband and multi-functional communications platforms [21]. Consequently, it is expected that a system having both the attractive Huygens radiation performance and an effective filtering function would be desirable if it could be made electrically small (i.e., $ka < 1$, where $k = 2\pi/\lambda_0$ and a is the radius of the smallest sphere that completely encloses the entire antenna system at the operational free-space wavelength λ_0). The resulting electrically small Huygens dipole filtenna (HDF) would be a multi-function system with non-interference performance characteristics. It would be quite suitable for many modern space-limited, portable, multiband wireless platforms.

Several effective methods have been developed to realize the out-of-band rejection functions of the filtennas. These include employing defected ground structures (DGSs) [12], utilizing multiple resonators [13-17], etching a U-shaped slot in the driven patch [18], and loading a stacked patch [19]. Unfortunately, they all have undesirable features, e.g., the requirement of large ground planes [12] or the need for many resonators, which would occupy large area [13-15] or a high profile [16-17]. Consequently, they are not suitable for electrically small filtenna designs, particularly when a ground plane is undesirable.

In this letter, an electrically small, low-profile, HDF is reported. An innovative finger-based interdigital capacitor (FIDC) structure is engineered to be seamlessly integrated into the magnetic near-field resonant parasitic (NFRP) element to empower it with good out-of-band rejection performance, while maintaining the HDA's good directional radiation performance characteristics and its electrically small package size. While similar in appearance to the radiating elements developed in [4], the novel FIDC-based CLL NFRP element enables these attractive spectral performance characteristics, which are significantly different from those of that dual-LP system. A prototype of this design was fabricated and measured, and the measured results are in good agreement with their simulated values. All of the numerical simulations and their optimization that are reported herein were performed using the finite-element-based, frequency domain ANSYS/ANSOFT high-frequency structure simulator (HFSS), version 20.0.

Manuscript received on September 3, 2021; revised on November 5, 2021, and on December 21, 2021; and accepted on December 22, 2021……

This work was supported in part by the National Natural Science Foundation of China contract number 62031006, in part by the Graduate Scientific Research and Innovation Foundation of Chongqing, China contract number CYB20066, in part by the Chongqing Natural Science Foundation contract number cstc2019jcyjjqX0004, and in part by the Australian Research Council grant number DP160102219. *(Corresponding author: Ming-Chun Tang.)*

Z. Wu and M.-C. Tang are with the Key Laboratory of Dependable Service Computing in Cyber Physical Society Ministry of Education, College of Microelectronics and Communication Engineering, Chongqing University, Chongqing 400044, China (E-mail: tangmingchun@cqu.edu.cn).

R. W. Ziolkowski is with the University of Technology Sydney, Global Big Data Technologies Centre, Ultimo NSW 2007, Australia (E-mail: Richard.Ziolkowski@uts.edu.au).

II. ELECTRICALLY SMALL HDF DESIGN

The geometric structure of the electrically small HDF is shown in Figs. 1(a) and 1(b). It consists of three substrate layers which all have the same radius: $R1$ = 35.0 mm, and 0.035 mm copper cladding thickness. Layer_1, Layer_2 are Taconic TLY-5 copper-cladded substrates (relative dielectric constant ε_r = 2.2, loss tangent tan δ = 0.0009, and substrate height $h1 = h2$ = 0.508 mm). Layer_3 is a Rogers Diclad 880 copper-cladded substrate (relative dielectric constant ε_r = 2.2, loss tangent tan δ = 0.0009, and substrate height $h3$ = 1.575 mm). They are supported with a 3D printed bracket.

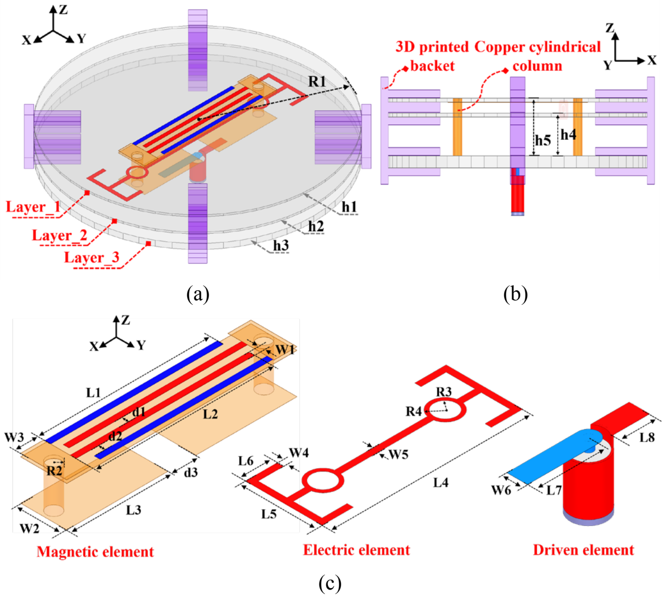

(a) (b)

(c)

Fig. 1. Configuration of the electrically small HDF. (a) 3-D isometric view. (b) Side view. (c) 3-D view of the magnetic and electric elements and driven element. The optimized design parameters (in millimeters): h1=0.508, h3=1.575, h4=5.55, h5=7.5, L1=41.0, L2=39.8, L3=22.25, L4=59.0, L5=12.2, L6=4.5, L7=11.0, L8=6.7, W1=0.5, W2=4.0, W3=4.0, W4=0.5, W5=0.2, W6=2.0, d1=0.6, d2=0.5, d3=4.9, R1=35.0, R2=1.25, R3=1.8, R4=2.4.

As shown in Fig. 1, the magnetic element is a capacitively loaded loop (CLL) integrated with two pairs of FIDCs. The copper patches of the CLL lie on the upper surface of Layer_3 and the lower surface of Layer_1. They are connected by two copper cylindrical columns, which pass through Layer_2. Each one has the height $h5$ and the radius $R2$. Fig. 1(c) shows two pairs of FIDC structures are placed on the upper surface of Layer_1. These finger copper strips are symmetrically located on both sides of the centerline of Layer_1. Two of the FIDC strips have the same size, $L2 \times W1$, along the x-axis, and the gap size between them is $d1$. The other two strips also have the same size, $L1 \times W1$, along the x-axis and are separated by the gap size $2 \times d2 + d1$. These FIDC strips are connected to the CLL on the lower surface of Layer_1 by a via with radius $R2$ that passes through Layer_1. The Egyptian axe dipole (EAD) is printed on the upper surface of Layer_2 and acts as the electric NFRP element. As Fig. 1(b) indicates, the vertical distance between the electric NFRP element and the upper surface of Layer_3 is $h4$. Two copper rings that have an inner radius $R3 > R2$ are integrated into the main strip of the EAD. The two copper cylindrical columns of the CLL pass completely through Layer_2 within them. This arrangement avoids the magnetic element being shorted to the EAD. A KTG 141–50 type, semi-rigid, 50 Ω coaxial cable was selected to feed the driven element, a simple dipole that lies on the bottom surface of Layer_3, as shown in Fig. 1(c).

A. Parametric Studies and Consequent Design Principles

The integration of the two pairs of FIDCs with the CLL NFRP element empowers the good out-of-band rejection performance of the HDF design. Parameter studies were performed on the corresponding CLL NFRP antenna to more clearly illustrate its filtering mechanisms and to make its design principles more clear and straightforward. They are explained through the evolutionary steps of the FDIC-based CLL NFRP design illustrated in Fig. 2(a). The corresponding simulated reflection coefficients, realized gain (RG) values and 3-D directivity patterns are shown in Figs. 2(b)-2(d).

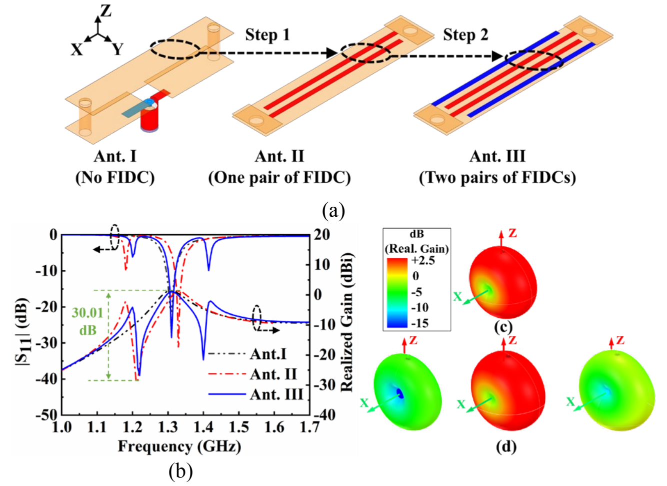

(a)

(b) (c) (d)

Fig. 2. Design evolution of the electrically small FIDC-based CLL NFRP antenna portion of the HDF. (a) Three design stages of its evolution. (b) Their simulated $|S_{11}|$ and realized gain values as functions of the source frequency. (c) 3-D directivity pattern of Ant. I at its resonance frequency. (d) 3-D directivity patterns of Ant. III at its resonance frequency and its two poles.

As illustrated in Fig. 2(a), Ant. I consists of a CLL NFRP element that is excited by the coax fed dipole [22]. Fig. 2(b) indicates that it achieves a resonance at 1.315 GHz with a 1.46 dBi peak RG. Moreover, the RG value witnesses only a gradual decrease at frequencies out of its passband. Figs. 2(c) and 2(a) show that Ant. I simply produces the LP field of a magnetic dipole without any filtering performance characteristics. A pair of strips (highlighted in red) is integrated above the CLL element of Ant. I to form the FIDC-based CLL NFRP Ant. II in Fig. 2(a). Fig. 2(b) indicates that Ant. II has a deep radiation null at 1.21 GHz. It also has a transmission pole at 1.182 GHz. Because of presence of the transmission zero at the lower frequency, 1.21 GHz, its out-of-band rejection level is improved there from 10.76 dB to 30.01 dB, i.e., a 19.25 dB enhancement.

In order to understand how the radiation null appears, an equivalent circuit model of Ant. II is presented in Fig. 3(a). As is known [23], the finger structure can be represented by a series inductance and capacitance, i.e., L_4 and C_{10}. The capacitive coupling between the fingers is modeled with the capacitance C_{12}. The term R_{rad} is the radiation resistance of Ant. II. The CLL NFRP element is represented by the combination of L_1, L_3 and the shunt resonant circuits composed of L_2 and C_1. The radiation resistance R_{rad} is simply replaced by a port with the same impedance to investigate the transmission response characteristics of the circuit [24]. The corresponding element values of the equivalent circuit were obtained through curve fitting and are detailed in Fig. 3.

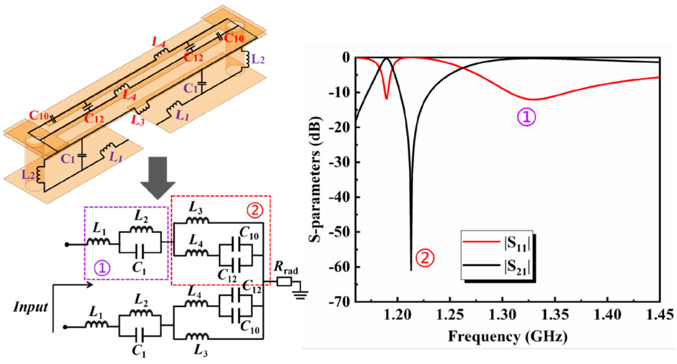

(a) (b)

Fig. 3. Equivalent circuit model of Ant. II. (a) Lumped elements corresponding to each part of Ant. II and the corresponding equivalent circuit model. (b) Simulated response for the equivalent circuit model. The circuit model parameters are: $L_1 = 12.7$ nH, $L_2 = 4.39$ nH, $L_3 = 9.1$ nH, $L_4 = 46$ nH, $C_1 = 4.37$ pF, $C_{10} = 0.042$ pF, $C_{12} = 0.27$ pF, and $R_{rad} = 30\ \Omega$.

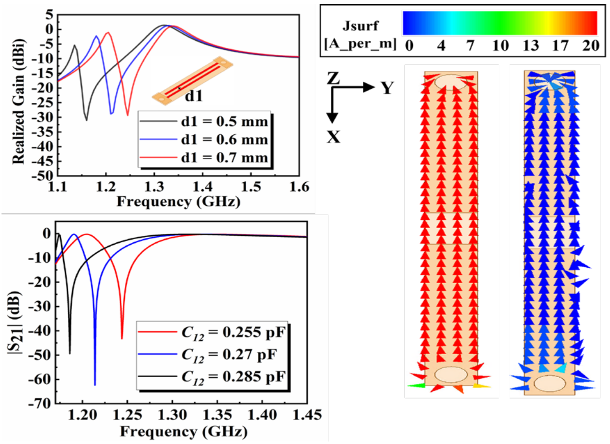

(a) (b) (c)

Fig. 4. Comparisons of the simulated realized gain values of Ant. II and the corresponding responses of the equivalent circuit model. (a) The distance *d1* between the FIDC strips and value of C_{12} of the equivalent circuit model are varied as a function of the source frequency. The current distributions on the upper surface of the CLL element of Ant. II at (b) the resonance frequency, 1.33 GHz, and (c) the frequency of the realized gain null, 1.21 GHz.

All of the circuit simulations were performed with Agilent's Advanced Design System (ADS) [25]. Fig. 3(b) plots the simulated $|S_{11}|$ and $|S_{21}|$ values of the equivalent circuit model of Ant. II with those component values. One transmission pole is present in the passband and one sharp transmission zero exists in the lower stopband together with a concomitant transmission pole. These characteristics agree well with the simulated values of the Ant. II. The tank circuit associated with L_1, L_2 and C_1 produces the transmission pole ①, while the tank circuit associated with L_3, L_4, C_{10} and C_{12} contributes the transmission zero ②. To verify this circuit explanation in the actual physical structure of the HDF, the distance *d1* between the FIDC strips was increased from 0.5 to 0.7 mm. A faster roll-off rate at the lower band edge is attained. This behavior is equivalent to a decrease in C_{12} as shown in Fig. 4(a).

In order to explain this outcome further, the current distributions on the upper surface of the CLL element of Ant. II are given in Figs. 4(b) and 4(c) at its resonance frequency, 1.33 GHz, and at the one null in the realized gain value, 1.21 GHz. As observed in Fig. 4(b), there is a strong and uniform current distribution on the radiating patch at the resonance frequency, which explains the high RG value, 1.31 dBi, of Ant. II in Fig. 4(a). On the other hand, the current distribution on the radiating patch at the radiation null in Fig. 4(c) is quite weak. This feature explains the very low realized gain level, -28.7 dBi, at the null frequency in Fig. 4(a).

Similar to Ant. II, Ant. III produces a radiation null out of the operating band at a higher frequency because of the presence of a second pair of copper strips, highlighted in blue in Fig. 2(a). The antenna has a 1.04 dBi peak RG at its operating center frequency, 1.31 GHz. The second pair of strips creates an additional radiation null at 1.4 GHz near its higher band edge. The out-of-band rejection level at the lower (higher) frequency band-edge is 27.64 (22.04) dB, a 17.91 (16.22) dB enhancement because of their presence. Both nulls are within 100 MHz of the center frequency.

Fig. 5 compares the prototype design (Des. I) with another optimized design (Des. II) whose nulls are yet closer. The FDIC length L1 in Des. II is varied to illustrate the ability to shift the upper null location. Des. II's center frequency is 1.27 GHz with L1 = 41.9 mm. Its realized gain curve has two deep nulls now at 1.22 and 1.34 GHz. It has improved frequency selectivity and out-of-band rejection levels in comparison to Des. I. Nevertheless, these filter enhancements come at the cost of a 0.98 dB decrease in the realized gain.

These results clearly demonstrate that the two radiation nulls are readily designed to be closer to the center frequency, particularly within 100 MHz, simply by adjusting the FIDCs parameters. Moreover, they illustrate the overall effects of having closer nulls on the HDF's overall performance. Additional simulation results indicate that the lower radiation null can be shifted within the frequency range 1.103 – 1.22 GHz and the higher one can be shifted within 1.34 – 1.494 GHz.

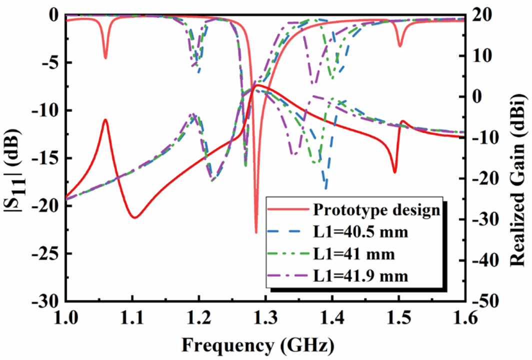

Fig. 5. Comparison of the prototype design's performance with another optimized design whose radiation nulls are closer to its center frequency. The FDIC's length L1 is varied in that alternate design.

III. SIMULATED AND MEASURED RESULTS

The prototype electrically small HDF was fabricated, assembled and measured. The prototype is shown in Fig. 6(a), which includes the assembled antenna and the sleeve balun introduced only for measurement purposes. The balun mitigates any spurious currents induced on the outer walls of the long coax cable and, hence, ensured the accuracy of the measurements of the impedance matching and the far-field directivity pattern characteristics [26].

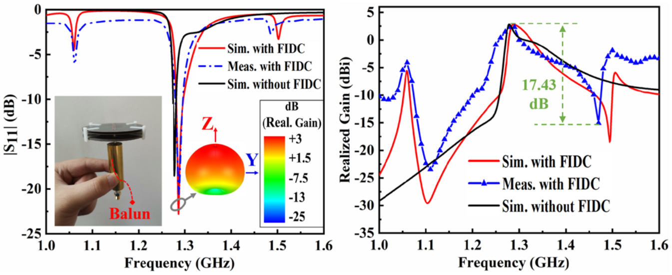

(a) (b)

Fig. 6. Simulated and measured performance of the electrically small HDF with and without the FIDC structures. (a) Simulated and measured $|S_{11}|$ values. (b) Simulated and measured realized gain values as functions of the source frequency.

The measured performance characteristics of the prototype system, together with their simulated values (taking into account of the presence of the balun), are presented in Figs. 6 and 7. As shown in Fig. 6(a), the simulated (measured) resonance frequency is centered at 1.286 (1.287) GHz with $|S_{11}|_{min}$ = -22.7 (-20.6) dB. The corresponding impedance bandwidth is 15 (15) MHz, from 1.281 (1.28) to 1.296 (1.295) GHz. It is clear from Fig. 6(b) that the simulated (measured) boresight realized gain has two deep nulls, respectively, at the lower 1.103 (1.11) GHz and higher 1.494 (1.47) GHz frequencies away from and surrounding the operational bandwidth. Note that in order to generate these nulls, two transmission poles are located at 1.06 (1.062) GHz and 1.502 (1.488) GHz and are associated with the poor impedance matching points indicated in Fig. 6(a). The corresponding simulated (measured) electrical size and total height of the prototype HDF at the resonant frequency were *ka* = 0.943 (0.943) and 0.0385 λ_0 (0.0385 λ_0), respectively. Because of the presence of the two radiation nulls, the measured (simulated) lower and upper band-edge rejection levels were 25.78 (32.27) dB and 17.43 (21.23) dB. These measured results are in good agreement with their simulated values, confirming that the high frequency rejection outside of the operating band of the system is obtained even with the electrically small size and low profile.

The simulated and measured RG patterns are given in Fig. 7. Because the simulated and measured cross-polarization levels in the E-plane are lower than –30 dBi, these patterns are visible only if the scale with –60 dB is used. Clearly, the antenna generated a Huygens source radiation pattern whose maximum is directed along the +*z*-axis. The simulated (measured) peak RG, FTBR, and overall efficiency (OE) values are 2.73 (2.33) dBi, 9.86 (8.45) dB, and 65.2% (63.1%), respectively. The 3 dB beam coverage was 113.6°, from -57° to 56.6° (104°, from -50° to 54°) in the E-plane (*x0y* plane) and 160.7°, from -80.4° to 80.3° (131°, from -63° to 68°) in the H-plane (*z0y* plane). Moreover, the simulated (measured) cross-polarization level in the broadside direction is below –63.2 (46) dB, indicating its high polarization purity.

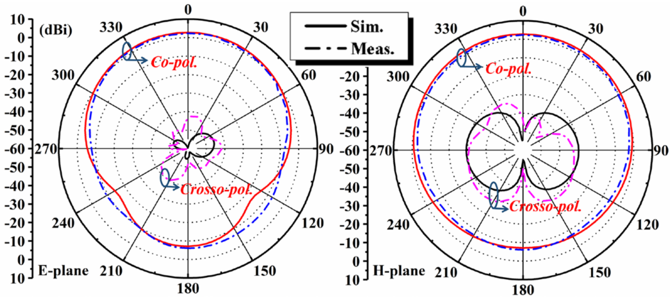

(a) (b)

Fig. 7. Simulated and measured 2-D realized gain patterns of the electrically small HDF operating at 1.286 (1.287) GHz. (a) E-plane. (b) H-plane.

Table I compares our HDF's performance with several reported filtennas. The volumes of the two filtennas reported in [12] and [19] were, respectively, $0.23 \times 10^{-1} \lambda_0^3$ (*ka* = 3.11) [12] and $0.2 \times 10^{-1} \lambda_0^3$ (*ka* = 2.81) [19]. The volume of our electrically small HDF, $0.27 \times 10^{-2} \lambda_0^3$, is 8.45 (7.35) times smaller than that in [12] ([19]). Despite its much smaller size, the peak RG value of our filtenna is only ~3.43 (~2.23) times smaller than that in [12] ([19]) and its band-edge selectivity is comparable. Moreover, in contrast with the omnidirectional radiating electrically small filtenna reported in [27], our HDF is broadside radiating without the presence of a ground plane.

TABLE I COMPARISON OF OUR HDF WITH REPORTED FILTENNAS

Ref.	*ka*	FBW (%)	RG (dBi)	Rejection Level (dB)	Directional Type
[12]	3.11	17.6	8.0	23.0 / 17.0	Uni
[19]	2.81	15.2	5.2	39.2 / 38.2	Uni
[27]	0.94	8.3	1.75	19.1 / 16.4	Omni
This work	0.94	1.2	2.33	25.78 / 17.43	Uni

IV. CONCLUSION

An electrically small, low-profile HDF, together with its design features and its performance characteristics, was reported. In particular, by loading a previously successful CLL-based NFRP element with a specially-engineered FIDC structure, the HDF reported herein displayed good out-of-band rejection performance for an electrically small size (*ka* = 0.943). Due to its compact size, high out-of-band rejection levels, and Huygens patterns with wide beamwidths, this electrically small HDF is a very good candidate for compact multi- band antenna systems needing multi-function, non-interfering, and radiating and receiving elements. For example, it would be ideal as elements for duplex systems such as those considered in [28], [29]. We have conducted further simulation studies to confirm this. In particular, we have found that when two of the developed electrically small HDFs are placed side-by-side with only a center-to-center separation of 27 mm (only 0.11 λ_{LB}) and the lower band (LB) one operates at 1.298 GHz and the higher band (HB) one operates at 1.397 GHz, this high-density duplex HDF configuration, whose frequency ratio is only 1.07, achieves a 33.3 dB and a 28.7 dB isolation level, respectively, in the LB and HB.

REFERENCES

[1] M.-C. Tang and R. W. Ziolkowski, “Efficient, high directivity, large front-to-back-ratio, electrically small, near-field-resonant-parasitic antenna,” *IEEE Access*, vol. 1, no. 1, pp. 16 - 28, May 2013.

[2] S. Lim and H. Ling, “Design of electrically small Yagi antenna,” *Electron. Lett.*, vol. 43, no. 5, pp. 3–4, Mar. 2007.

[3] P. Jin and R. W. Ziolkowski, “Metamaterial-inspired, electrically small Huygens sources,” *IEEE Antennas Wirel. Propag. Lett.*, vol. 9, pp. 501-505, 2010.

[4] M.-C. Tang, Z. Wu, T. Shi, H. Zeng, W. Lin, and R. W. Ziolkowski, “Dual-linearly polarized, electrically small, low-profile, broadside radiating, Huygens dipole antenna,” *IEEE Trans. Antennas Propag.*, vol. 66, no. 8, pp. 3877–3885, Aug. 2018.

[5] P. Alitalo, A. O. Karilainen, T. Niemi, C. R. Simovski, and S. A. Tretyakov, “Design and realisation of an electrically small Huygens source for circular polarisation,” *IET Microw., Antennas Propag.*, vol. 5, no. 7, pp. 783–789, May 2011.

[6] W. Lin and R. W. Ziolkowski, “Electrically-small, low-profile, Huygens circularly polarized antenna,” *IEEE Trans. Antennas Propag.*, vol. 66, no. 2, pp. 636-643, Feb. 2018.

[7] P. F. Hu, Y. M. Pan, and B. Hu, “Electrically small, planar, complementary antenna with reconfigurable frequency,” *IEEE Trans. Antennas Propag.*, vol. 67, no. 8, pp. 5176-5184, Aug. 2019.

[8] Z. Wu, M.-C. Tang, M. Li, and R. W. Ziolkowski, “Ultralow-profile, electrically small, pattern-reconfigurable metamaterial-inspired Huygens dipole antenna,” *IEEE Trans. Antennas Propag.*, vol. 68, no. 3, pp. 1238-1248, Mar. 2020.

[9] M.-C. Tang, T. Shi, and R. W. Ziolkowski, “Electrically small, broadside radiating Huygens source antenna augmented with internal non-Foster elements to increase its bandwidth,” *IEEE Antennas Wirel. Propag. Lett.*, vol. 16, pp. 712-715, 2017.

[10] S. Lee, G. Shin, S. M. Radha, J. Choi, and I. Yoon, “Low-profile, electrically small planar Huygens source antenna with an endfire radiation characteristic,” *IEEE Antennas Wirel. Propag. Lett.*, vol. 18, no. 3, pp. 412-416, Mar. 2019.

[11] W. Lin, R. W. Ziolkowski, and J. Huang, “Electrically small, low-profile, highly efficient, Huygens dipole rectennas for wirelessly powering internet-of-things devices,” *IEEE Trans. Antennas Propag.*, vol. 67, no. 6, pp. 3670-3679, Jun. 2019.

[12] W. Yang, S. Chen, Q. Xue, W. Che, G. Shen, and W. Feng, “Novel filtering method based on metasurface antenna and its application for wideband high-gain filtering antenna with low profile,” *IEEE Trans. Antennas Propag.*, vol. 67, no. 3, pp. 1535-1544, Mar. 2019.

[13] K. Dhwaj, H. Tian, and T. Itoh, “Low-profile dual-band filtering antenna using common planar cavity,” *IEEE Antennas Wireless Propag. Lett.*, vol. 17, no. 6, pp. 1081–1084, Jun. 2018.

[14] C. X. Mao, S. Gao, Y. Wang, and Z. Cheng, “Filtering antenna with two-octave harmonic suppression,” *IEEE Antennas Wireless Propag. Lett.*, vol. 16, pp. 1361–1364, 2017.

[15] X. Chen, F. Zhao, L. Yan, and W. Zhang, “A compact filtering antenna with flat gain response within the passband,” *IEEE Antennas Wireless Propag. Lett.*, vol. 12, pp. 857–860, 2013.

[16] H. Cheng, Y. Yusuf, and X. Gong, “Vertically integrated three-pole filter/antennas for array applications,” *IEEE Antennas Wireless Propag. Lett.*, vol. 10, pp. 278–281, 2011.

[17] L.-S. Wu, Y.-X. Guo, J.-F. Mao, and W.-Y. Yin, “Design of a substrate integrated waveguide balun filter based on three-port coupled-resonator circuit model,” *IEEE Microw. Wireless Compon. Lett.*, vol. 21, no. 5, pp. 252–254, May 2011.

[18] X. Y. Zhang, W. Duan, and Y. Pan, “High-gain filtering patch antenna without extra circuit,” *IEEE Trans. Antennas Propag.*, vol. 63, no. 12, pp. 5883-5888, Dec. 2015.

[19] B. Zhang and Q. Xue, “Filtering antenna with high selectivity using multiple coupling paths from source/load to resonators,” *IEEE Trans. Antennas Propag.*, vol. 66, no. 8, pp. 4320-4325, Aug. 2018.

[20] K. Xue, D. Yang, C. Guo, H. Zhai, H. Li, and Y. Zeng, “A dual-polarized filtering base-station antenna with compact size for 5G applications,” *IEEE Antennas Wireless Propag. Lett.*, vol. 19, no. 8, pp. 1316-1320, Aug. 2020.

[21] Y. Lee, J. Tarng, and S. Chung, “A filtering diplexing antenna for dual-band operation with similar radiation patterns and low cross-polarization levels,” *IEEE Antennas Wireless Propag. Lett.*, vol. 16, pp. 58-61, 2017.

[22] P. Jin and R. W. Ziolkowski, “Multi-frequency, linear and circular polarized, metamaterial-inspired, near-field resonant parasitic antennas,” *IEEE Trans. Antennas Propag.*, vol. 59, no. 5, pp. 1446-1459, May 2011.

[23] B. Zong, H. Zeng, F. Wu, G. Wang, and L. Geng, “Wide-angle frequency-scanning array antenna using dual-layer finger connected interdigital capacitor based CRLH unit cell,” *IEEE Access*, vol. 9, pp. 35957-35967, Mar. 2021.

[24] W. Duan, X. Y. Zhang, Y.-M. Pan, J. X. Xu, and Q. Xue, “Dual-polarized filtering antenna with high selectivity and low cross polarization,” *IEEE Trans. Antennas Propag.*, vol. 64, no. 10, pp. 4188–4196, Oct. 2016.

[25] Advanced Design System (ADS). [Online]. Available: http://www.keysight.com.

[26] S. A. Saario, J. W. Lu, and D. V. Thiel, “Full-wave analysis of choking characteristics of sleeve balun on coaxial cables,” *Electron. Lett.*, vol. 38, no. 7, pp. 304–305, Mar. 2002.

[27] M.-C. Tang, Y. Chen and R. W. Ziolkowski, “Experimentally validated, planar, wideband, electrically small, monopole filtennas based on capacitively loaded loop resonators,” *IEEE Trans. Antennas Propag.*, vol. 64, no. 8, pp. 3353-3360, Aug. 2016.

[28] C.-X. Mao, S. Gao, and Y. Wang, “Dual-band full-duplex Tx/Rx antennas for vehicular communications,” *IEEE Trans. on Veh. Technol.*, vol. 67, no. 5, pp. 4059-4070, May 2018.

[29] C.-X. Mao, S. Gao, Y. Wang, Y. Liu, X.-X. Yang, Z.-Q. Cheng, and Y .-L. Geng, “Integrated dual-band filtering/ duplexing antennas,” *IEEE Access*, vol. 6, pp. 8403-8411, Feb. 2018.